

# Towards Biowastes Valorization. Peanut Shell as Resource for Quality Chemicals and Activated Biochar Production.

Carla Soledad Fermanelli (✉ [cfermanelli@frc.utn.edu.ar](mailto:cfermanelli@frc.utn.edu.ar))

Unidad de Fitopatología y Modelización Agrícola (UFYMA) <https://orcid.org/0000-0003-3136-5187>

Adrián Chiappori

Centro de Investigación y Tecnología Química (CITeQ)

Liliana B. Pierella

Centro de Investigación y Transferencia en Acústica

Clara Saux

Centro de Investigación y Tecnología Química

---

## Research

**Keywords:** peanut shell, biomass pyrolysis, biooil upgrade, Ni-ZSM-11, activated biochar

**Posted Date:** June 29th, 2021

**DOI:** <https://doi.org/10.21203/rs.3.rs-632811/v1>

**License:**  This work is licensed under a Creative Commons Attribution 4.0 International License.

[Read Full License](#)

---

**Version of Record:** A version of this preprint was published at Sustainable Environment Research on January 8th, 2022. See the published version at <https://doi.org/10.1186/s42834-021-00112-9>.

1       **Towards biowastes valorization. Peanut shell as resource for**  
2       **quality chemicals and activated biochar production.**

3       Carla S. Fermanelli<sup>1\*</sup>, Adrián Chiappori<sup>2</sup>, Liliana B. Pierella<sup>3</sup>, Clara Saux<sup>2</sup>

4       <sup>1</sup>Unidad de Fitopatología y Modelización Agrícola (UFYMA), INTA – CONICET. Camino  
5       60 cuadras km 5 ½, Córdoba, Argentina.

6       <sup>2</sup>Centro de Investigación y Tecnología Química (CITeQ), UTN – CONICET. Maestro  
7       López esq. Cruz Roja Argentina, (5016) Córdoba, Argentina.

8       <sup>3</sup>Centro de Investigación y Transferencia en Acústica (CINTRA), UTN – CONICET.  
9       Maestro López esq. Cruz Roja Argentina (5016), Córdoba, Argentina.

10      \*Correspondence: [cfermanelli@frc.utn.edu.ar](mailto:cfermanelli@frc.utn.edu.ar) (C.S. Fermanelli)

## 11 ABSTRACT

12 The purpose of this work was to valorize a regional biowaste through a modest thermo-  
13 catalytic pyrolysis process. ZSM-11 zeolites modified by Ni incorporation (1-8 wt%) were  
14 synthesized and characterized by means of X-Ray Diffraction, Inductively Coupled Plasma  
15 Atomic Emission Spectroscopy, Infrared Fourier Transform Spectroscopy, UV–vis Diffuse  
16 Reflectance Spectra and Temperature Programmed Reduction. Results demonstrated that Ni  
17 was mainly incorporated as oxide. These porous materials were evaluated as heterogeneous  
18 catalysts to improve biooil composition. In this sense, higher hydrocarbon yields and quality  
19 chemicals were obtained and oxygenates were diminished. The deactivation of the most  
20 active material was studied over six cycles of reaction. In order to achieve the circular  
21 bioeconomy postulates, the obtained biochar (usually considered a residue) was further  
22 valorized through a physicochemical activation. The obtained activated biochars were  
23 extensively characterized.

24 **Keywords:** peanut shell, biomass pyrolysis, biooil upgrade, Ni-ZSM-11, activated biochar.

## 25 1. Introduction

26 In its 17 Sustainable Development Goals (SDGs), the United Nations promotes the  
27 principle of optimum and responsible usage of resources for purposes leading to a convincing  
28 transition to a circular economy. The main idea of the so-called circular economy consists in  
29 advanced redesigning and technological breakthroughs to minimize waste [1]. From these  
30 ideas, the concept of “circular bioeconomy” is proposed to be a more efficient biobased  
31 renewable resource management. This term integrates the circular economy principles with  
32 the bioeconomy theory [2].

33 Biomass is a promising alternative to fossil resources since its carbon richness. But  
34 considering its importance for food production, a competitive situation should be avoided. In  
35 this sense, agricultural wastes are ideal candidates for fuels and chemicals production. Peanut  
36 is an important grain legume cultivated worldwide with a growing trend of production of  
37 about 48 million tonnes [3]. Argentina is the 8<sup>th</sup> world peanut producer, with around 1,3  
38 million tonnes produced in 2019/2020 campaign. In view of these high quantities, it is  
39 important to consider the wastes that peanut processing generates. A 25 wt% of the  
40 production corresponds to the shell, a by-product not properly used. Keeping in mind the  
41 concept of circular economy, peanut shell (PS) could be consider as the feed of an integral  
42 process.

43 PS contains around 50% cellulose, 20% hemicellulose and 30% lignin [4] that make it  
44 difficult to digest and unable as feedstock for animals. Furthermore, biodegradation is  
45 extremely low, resulting in the need of severe treatments. Hence, fast pyrolysis seems to be  
46 a good alternative in order to treat and give value to this biowaste. In a previous paper [5] we  
47 have shown the importance of this thermal process.

48 As proposed by Dai et al. [6] the use of zeolites as catalysts in pyrolysis reactions could  
49 improve hydrocarbons and aromatics yields. Particularly, they have found that Ni modified  
50 zeolites promoted pyrolysis vapor deoxygenation and selectivity to aromatic compounds.  
51 The use of Ni promoted catalysts in biomass pyrolysis has been studied by many researchers.  
52 Most studies focused on ZSM-5, MCM or different oxides [7], but the use of Ni modified  
53 ZSM-11 zeolite has hardly been investigated.

54 As in any production system, biomass fast pyrolysis also generates waste. The solid  
55 product of pyrolysis, commonly known as biochar is usually disposed of and not further  
56 utilized. Taking Olofsson and Börjesson [8] ideas, and in order to minimize residues  
57 generation, we propose a case of open-loop recycling by employing the biochar in a  
58 subsequent system: synthesis of activated biochar (AB). This porous material can be used in  
59 Li-ion batteries, gas-phase adsorption or as heterogeneous catalysis.

60 In this paper, we propose the valorization and recycling of PS in two subsequent  
61 product systems. In the first system, PS is considered as renewable C source for platform  
62 molecules generation. Considering this biowaste composition, a thermo-catalytic pyrolysis  
63 method is proposed. In order to obtain higher hydrocarbons and aromatics yields in the biooil,  
64 the effect of Ni-ZSM-11 catalyst is evaluated. The second system employs the residue from  
65 the previous one, that is to say biochar, for the synthesis of AB (**Figure 1**).

## 66 **2. Experimental section**

### 67 **2.1. Biomass**

68 PS was provided by the company Lorenzati, Ruetsch y Cia., from Córdoba, Argentina.  
69 The following pre-treatments were applied to PS: (1) washing to remove soil particles, (2)  
70 drying at 105 °C until constant weight, (3) grinding and (4) screening to obtain a PS particle  
71 size < 3.35 mm –ASTM E 11/95–. Detailed characterization of biomass has been presented  
72 in a previous work [5].

### 73 **2.2. Catalysts synthesis and characterization**

74 The microporous Na-ZSM-11 zeolite (Si/Al = 23) was prepared by hydrothermal  
75 synthesis [9]. Ni-zeolites were prepared by the wet impregnation method. Three  
76 concentrations of nickel aqueous solutions ( $NiCl_2 \cdot 6H_2O$ , Cicarelli) were used to reach a Ni-  
77 content of 1, 5 and 8 wt%. The zeolite was dispersed in the Ni solution at room temperature.  
78 Afterwards, the solvent (water) was slowly removed by rotary vacuum evaporation at 80 °C  
79 until complete dryness. Finally, the samples were dried at 110 °C overnight and subjected to  
80 a thermal treatment consisting of desorption in  $N_2$  and calcination in air at 500 °C for 8 h.  
81 The as-prepared catalysts were named Ni(1)Z, Ni(5)Z and Ni(8)Z, according to metal  
82 concentration.

83 Nickel content was determined by inductively coupled plasma atomic emission  
84 spectroscopy with an ICP–OPTIMA Perkin Elmer equipment. The crystalline structure of  
85 the catalysts was determined by means of X-ray diffraction (XRD) employing an X’pert  
86 PANalytical diffractometer with  $CuK\alpha$  radiation (1.54 Å). The data were collected in 2 $\theta$   
87 range of 5 – 60° in steps of 0.026° with a count time of 2 s at each point.

88 Surface area determinations ( $S_{BET}$ ) using Brunauer–Emmett–Teller (BET) method  
89 were carried out with  $N_2$  absorption at 77 K in a Pulse Chemisorb equipment Micromeritics  
90 2700. The  $S_{BET}$  was determined for fresh and spent catalysts (after the reaction).

91 Temperature programmed reduction (TPR) studies were done over Ni-zeolites in a  
92 Pulse Chemisorb 2720 equipment from Micromeritics. UV–vis diffuse reflectance spectra  
93 (UV–vis DRS) in absorbance mode were recorded using a Jasco V 650 spectrometer in the  
94 wavelength range 200 to 900 nm.

95 Infrared Fourier Transform Spectroscopy (FTIR) studies were done to determine  
96 acidity of catalysts, employing a Thermo Nicolet iS10. Pyridine was first adsorbed to the  
97 materials at room temperature under vacuum conditions and was further desorbed at 250 °C  
98 and 10<sup>-4</sup> Torr. Acids sites quantification was done from the bands of 1545 cm<sup>-1</sup> (Brønsted)  
99 and 1450 cm<sup>-1</sup> (Lewis) using the literature data of the integrated molar extinction coefficients  
100 [10].

101 The amount of coke deposited on the spent catalysts was measured by  
102 thermogravimetric analysis (TGA) using a Mettler Toledo thermobalance  
103 (TGA/SDTA851e/SF/1100°C). The sample was heated from 25 to 900 °C at a heating rate  
104 of 10 °C min<sup>-1</sup> under 75 mL min<sup>-1</sup> of air flow. Eq. (1) was used to calculate the relative  
105 amount of coke [11].

$$106 \quad Y_{coke} (wt\%) = \frac{m_{100^{\circ}C} - m_{900^{\circ}C}}{m_{900^{\circ}C}} \cdot 100 \quad \text{Eq. (1)}$$

107 Where  $m_{100^{\circ}C}$  and  $m_{900^{\circ}C}$  correspond to the catalyst mass at 100 °C and 900 °C,  
108 respectively.

109 Functional structure of spent catalysts was characterized by XRD and FTIR using the  
110 equipment depicted above. In the case of FTIR, the KBr technique was employed.

### 111 **2.3. Pyrolysis reactions**

112 PS pyrolysis and biooil upgrade were simultaneously carried out in a fixed bed glass  
113 reactor (23 mm I.D., 290 mm length) under N<sub>2</sub> flow (60 mL min<sup>-1</sup>). For a typical experiment,  
114 PS (1 g) was loaded in a glass sample carrier over a catalytic bed. The bed consisted of  
115 catalyst (1 g) and milled quartz (7 g). The reactor was introduced in an electric furnace once

116 the pyrolysis temperature (500 °C) was reached. Condensable vapors were collected at the  
117 reactor output in a condenser (<-10 °C). The reactions lasted 10 min. Three repeats of every  
118 experimental run were done. Average values are reported.

119 Eqs. (2), (3) and (4) were used to calculate products yields.

$$120 \quad Y_{biochar} (wt\%) = \frac{M_{biochar}}{M_o} \cdot 100 \quad \text{Eq. (2)}$$

$$121 \quad Y_{biooil} (wt\%) = \frac{M_{bio-oil}}{M_o} \cdot 100 \quad \text{Eq. (3)}$$

$$122 \quad Y_{gas} (wt\%) = 100 - [Y_{biooil} + Y_{bio-char} + Y_{coke}] \quad \text{Eq. (4)}$$

123 Where,  $M_o$  is the initial mass of the biomass sample (g),  $M_{biochar}$  is the mass of the  
124 solid product (g) after the reaction and  $M_{biooil}$  is the mass of the liquid product (g).

125 Catalyst stability was assessed by using one catalyst sample for six consecutive  
126 reaction cycles. Every new reaction was carried out employing the catalyst from the  
127 preceding cycle (i.e., the partially deactivated catalyst) maintaining the 1:1 biomass to  
128 catalyst mass ratio. Biooil was collected and analyzed after each reaction cycle.

## 129 **2.4. Products analysis and characterization**

130 Chemical composition of biooil was assessed by the GC-MS technique in a Perkin  
131 Elmer Claurus 600 Gas Chromatograph coupled with an ion trap mass spectrometer in full  
132 scale mode (m/z 40 to 550). An Elite 5MS capillary column (30 m length, 0.25 mm i.d.) was  
133 employed and He was used as carrier gas. Chromatographic peaks were identified by means  
134 of NIST MS library and the use of standards. Peak area calibration was accomplished through

135 specific response factors for each chemical group. The selectivity to each compound was  
136 calculated using Eq. (5):

$$137 \quad S_i(\%) = \frac{A_i \cdot R_i}{\sum_{i=1}^n A_i \cdot R_i} \times 100 \quad \text{Eq. (5)}$$

138 Where  $A_i$  is the absolute peak area of compound  $i$  and  $R_i$  is the response factor of  
139 compound  $i$ .

## 140 **2.5. Activated biochar synthesis and characterization**

141 AB synthesis was carried out following the protocol published by Fu et al. [12], due to  
142 its simplicity and effectiveness. A mechanical mixture of KOH (Strem Chemicals, 85%) and  
143 biochar was made in the proportions of 1:1 and 3:1 by weight. The mixture was placed in a  
144 fixed bed reactor and submitted to thermal treatment under N<sub>2</sub> atmosphere (20 mL min<sup>-1</sup>).  
145 The heating rate was 20 °C min<sup>-1</sup> until 750 °C, maintaining that temperature for 3 h. The as-  
146 prepared materials, named AB 1:1 and AB 3:1, were then neutralized and washed with  
147 distilled water until pH=7 and dried in an oven at 120 °C until constant weight.

148 AB yields were calculated employing Eq. (6), where  $M_{biochar}$  corresponds to the mass  
149 of the biochar (g) after the pyrolysis reaction,  $M_{AB}$  is the mass of the as-prepared activated  
150 biochar (g) after the synthesis procedure.

$$151 \quad Y_{AB} (wt\%) = \frac{M_{AB}}{M_{biochar}} \cdot 100 \quad \text{Eq. (6)}$$

152 The crystalline structure, FTIR spectra and S<sub>BET</sub> of AB were determined in the  
153 equipment depicted above. For FTIR analysis, the samples were prepared by blending a few  
154 milligrams of the AB sample with KBr.

155 Morphological analyses were done by Scanning Electron Microscopy (SEM)  
156 employing a microscope FE-SEM Sigma. It was operated at an acceleration voltage of 5 kV.  
157 Prior to analysis, the samples were coated with gold. Proximate analysis of AB was also  
158 performed using the thermobalance depicted above and following Saldarriaga et al., [13]  
159 protocol.

160 A LabRam spectrometer (Horiba-Jobin-Yvon) coupled to an Olympus confocal  
161 microscope was used to obtain the Raman spectra of AB samples. The spectrometer was  
162 equipped with a CCD detector at  $\sim 200$  K, the excitation wavelength was 532 nm and the  
163 laser power was set at 30 mW.

### 164 3. Results and discussion

#### 165 3.1. Catalysts characterization

166 The physicochemical properties of the catalysts are shown in **Table 1**. It can be seen  
167 that surface area of fresh materials varied as a function of Ni content. In general, when metal  
168 is loaded on porous supports, the surface area decreases due to the pore blockage and metal  
169 sintering during the calcination step [14].  $S_{\text{BET}}$  for spent catalysts showed a 23-35% decrease,  
170 compared to the fresh samples. It was observed that the reduction in  $S_{\text{BET}}$  was bigger when  
171 greater the initial  $S_{\text{BET}}$  was.

172 The ICP analysis of the materials confirmed the theoretical Ni quantities, which were  
173 in agreement with the experimental results.

**Table 1.** Physicochemical characteristics of the catalysts.

Catalyst	Ni <sup>a</sup>	$S_{\text{BET}}$ (m <sup>2</sup> g <sup>-1</sup> )	Lewis	Brønsted	Total acidity
----------	-----------------	--	-------	----------	---------------

	(%wt)	Fresh	Spent	( $\mu\text{mol Py mg}^{-1}$ )	( $\mu\text{mol Py mg}^{-1}$ )	( $\mu\text{mol Py mg}^{-1}$ )
HZ	0.00	378	249	7.69	68.79	76.48
Ni(1)Z	0.76	331	260	49.30	61.60	110.91
Ni(5)Z	5.40	321	221	97.97	124.42	222.39
Ni(8)Z	7.40	287	221	52.62	54.68	107.30

174 <sup>a</sup> Determined by ICP.

175 The FTIR spectra of the Ni-zeolites samples desorbed at 250 °C are shown in **Figure**  
176 **2a**. Bands at 1455, 1492 and 1545  $\text{cm}^{-1}$  can be observed. The band at 1545  $\text{cm}^{-1}$  corresponds  
177 to the BAS (Brønsted Acid Sites) formed by the framework Al species through the Si – OH  
178 – Al bridge. This band is ascribed to the interaction of pyridinium ion binding on BAS. The  
179 band at 1450  $\text{cm}^{-1}$  is related to the LAS (Lewis Acid Sites) formed by the extra framework  
180 Al species and electronic defaults in the framework aluminium [15]. The band at 1492  $\text{cm}^{-1}$   
181 corresponds to the vibration of pyridine adsorbed over both LAS and BAS [16].

182 From **Table 1** and **Figure 2a** it can be seen that the total amount of LAS increased  
183 dramatically when the Ni was incorporated to the pristine zeolites. It is well known that the  
184 addition of Ni to zeolites modify the acidic properties of the material [17]. The metal can  
185 create new LAS associated with  $\text{Ni}^{2+}$  and NiO. The highest LAS amount was observed in the  
186 sample Ni(5)Z, in accordance to the literature, for similar zeolites [18]. After Ni  
187 incorporation, BAS slightly decreased in the case of the Ni(1)Z sample, but were significantly  
188 augmented in the case of the Ni(5)Z catalyst. On further increase of the metal content to 8  
189 wt%, a reduction in both LAS and BAS quantification was observed. This phenomenon could  
190 be a consequence of the inaccessibility of pyridine to some of these sites as result of the pore

191 blockage caused by the larger oxide particles. In any case, the total amount of acid sites  
192 increased in all modified samples compared with the parent zeolite.

193 The XRD patterns of the catalytic materials presented in **Figure 2(b)** confirmed the  
194 ZSM-11 structure for all the zeolites. In this way, it was possible to observe the characteristic  
195 signals at  $2\theta$  of  $7 - 9^\circ$  and  $23 - 24^\circ$  [19]. The diffraction pattern of NiO was also incorporated  
196 in this figure and the presence of its characteristic signals was emphasized. The intensity of  
197 these peaks increased when the amount of the metal incorporated augmented.

198 Results of reducibility of Ni species are presented in **Figure 2c**. All samples presented  
199 similar profiles, consisting mainly of a peak centered around  $350 - 400^\circ\text{C}$ , while Ni(8)Z  
200 exhibited another broad peak at around  $550^\circ\text{C}$ . The intensity and peak area of the Ni-zeolites  
201 spectra increased with Ni contents. The peak centered at lower temperatures corresponds to  
202 the highly dispersed Ni species, which have weak interactions with the support [20]. This  
203 peak can be attributed to the reduction of NiO to metallic nickel. It is noticeable that at higher  
204 metal content the signal became wider as consequence of diffusional limitations for bigger  
205 oxide particles. The second peak, centered at higher temperatures, can be assigned to Ni  
206 species with stronger interaction with the zeolite surface [18]. It is possible to infer that these  
207 species are also present in Ni(5)Z, but they are more prominent at higher metal content.

208 **Figure 2d** presents DRS UV-Vis spectra of the samples in order to verify the chemical  
209 environment of Ni present on them. As observed, the HZ spectrum presents a band at 200  
210 nm that could be assigned to Al-O charge-transfer transition of four-coordinated framework  
211 Al, while the shoulder at 250 nm has been assigned to highly ordered structures with  
212 octahedral symmetry [21]. All Ni modified samples present the characteristic band of NiO

213 around 300 nm. In the case of Ni(8)Z there is a shift in this band to higher wavelength that  
214 may correspond to higher oxide particles [22], in accordance with XRD and TPR results.  
215 This observation confirmed the previous analysis made for the acid sites of the materials.  
216 Ni(8)Z, as consequence of the higher metal content presents the biggest oxide particles that  
217 blocks some pore's mouths. Thus, internal acid sites became inaccessible. For this sample,  
218 bands at 390, 429 and 725 nm, characteristic of NiO, became more evident and their intensity  
219 increased as Ni content was higher.

220 Even when NiO is predominant in all the Ni-samples, there are also some absorption  
221 bands assigned to Ni<sup>2+</sup> octahedrally coordinated (410, 650 and 740 nm) [23] indicating the  
222 coexistence of both species.

### 223 **3.2. Catalytic activity**

224 In order to determine Ni loading effect in ZSM-11 catalytic activity for biomass  
225 pyrolysis, a series of experiments were performed. **Table 2** presents the mass balance of PS  
226 pyrolysis reactions catalyzed by the studied materials. As can be observed, biooil yields were  
227 similar in Ni(5)Z and Ni(8)Z catalyzed reactions. Nevertheless, a slight reduction in the biooil  
228 yield was verified when HZ and Ni(1)Z zeolites were employed. This result is a consequence  
229 of the increased selectivity towards permanent gases that occurs during the cracking of longer  
230 chain molecules.

231 With respect to biochar yield, it ranged around 29-30 wt%. These small variations  
232 were mainly caused by experimental error and the natural heterogeneity of PS. Considering  
233 the experimental set up, only pyrolysis vapors pass through the catalytic bed, so this  
234 observation could not be ascribed to a catalytic effect.

235 When analyzing coke yields, it was observed that the parent zeolite registered the  
 236 highest coke deposition among the studied materials, suggesting that Ni incorporation to  
 237 ZSM-11 zeolites prevents the formation of these carbonaceous products. This result is in  
 238 agreement with Stanton et al. [24] who found that Ni-modified ZSM-5 zeolites generated  
 239 lower coke deposits, compared with the unmodified fresh ZSM-5 catalyst. It is well known  
 240 that coke deposits over catalysts can be generated by (1) polymerization of phenolic  
 241 compounds (called thermal origin) and (2) transformation of oxygenated compounds over  
 242 catalyst acid sites (called catalytic origin) [25]. Catalysts properties like porosity, particle  
 243 size and surface area play an important role in coke formation [26].

**Table 2.** Mass balance of PS pyrolysis reactions catalyzed with Ni-zeolites

	Biooil	Biochar	Gas	Coke
Thermal	50.76 ± 2.54	28.56 ± 1.43	20.68 ± 1.03	
HZ	47.81 ± 2.39	27.54 ± 1.38	17.42 ± 0.87	7.23 ± 0.36
Ni(1)Z	44.76 ± 2.24	29.32 ± 1.47	21.22 ± 1.06	4.71 ± 0.24
Ni(5)Z	49.97 ± 2.50	30.33 ± 1.51	15.28 ± 0.76	4.44 ± 0.22
Ni(8)Z	50.37 ± 2.52	28.94 ± 1.45	14.75 ± 0.74	5.94 ± 0.30

### 244 3.3. Biooil upgrade

245 The effects of the Ni modified zeolites on the product distribution of PS pyrolysis is  
 246 presented in **Figure 3**. Compounds found in the biooil were classified into oxygenated  
 247 compounds (acids, aldehydes, ketones, phenols, alcohols, furans and esters) and  
 248 hydrocarbons (aliphatics and aromatics). As can be observed, O-containing compounds were  
 249 the main products in the thermal pyrolysis of PS. As expected, when Ni-zeolites were

250 employed, O-containing compounds decreased while hydrocarbons selectivity increased.  
251 Considering the reactor disposal, once the pyrolysis occurred, the vapors came in contact with  
252 the solid catalyst. Active sites are present on the surface and in the pores of the zeolites. When  
253 pyrolysis products make contact with them, reactions such as cracking, isomerization,  
254 aromatization and polymerization occurred. Thus, selectivity towards hydrocarbons  
255 increased. The main compounds identified were similar to those reported in literature [6] and  
256 they are listed in **Table S1**, in the Supporting Information file.

257 Biooils from all catalyzed reactions presented higher concentration of hydrocarbons  
258 than the thermal run. Ni(1)Z and Ni(8)Z catalysts presented lower hydrocarbons selectivity  
259 than the parent HZ zeolite. While, Ni(5)Z showed considerable deoxygenation and the  
260 highest hydrocarbons selectivity. This behavior suggests that there would be an optimal  
261 amount of metal to incorporate on a determined zeolite matrix. Kostyniuk et al. [18] found  
262 that zeolites with 5 wt% of Ni were the most active catalysts in hydrogenation, hydrocracking  
263 and isomerization reactions of biomass tar model compound mixture. It has been proposed  
264 that the impregnation of the catalyst with nickel significantly improved the selectivity  
265 towards hydrocarbons in the biooil from pyrolysis of lignocellulosic biomass [27]. The nickel  
266 particles strongly promote the hydrogen-transfer reactions that favor the formation of  
267 hydrocarbons during the catalytic improvement of the pyrolysis vapors [28].

268 It should be noted that the hydrocarbon fraction was mainly composed by aromatics  
269 (**Figure 3b**). It is well known that aromatization reactions require synergies of Brønsted and  
270 Lewis acid sites. Although BAS are active sites for aromatization reactions, dehydrogenation  
271 or hydrogen atom transfer reaction occurs on the LAS [29]. As presented in **Table 1** Ni(5)Z

272 zeolite had the highest LAS and BAS. Consequently, lowest oxygenated compounds and  
273 highest aromatic selectivities were obtained over this material.

274 **Figure 3c** shows hydrocarbons distribution in the liquid products, according to the  
275 number of C-atoms per molecule. As can be observed, selectivity towards C10–C15  
276 compounds was extremely low in the studied reactions.

277 On the contrary, Ni(5)Z favored the cracking to yield higher amounts of low molecular  
278 weight compounds, with 7–9 carbon atoms per molecule. This group includes valuable  
279 products like xylenes (C8), cumene and trimethylbenzene –TMB– (C9). Less valuable  
280 toluene (C7) was also present in the analyzed biooil. Nevertheless, the petrochemical industry  
281 can convert toluene to those important products by aromatic hydrocarbons transformations  
282 reactions. Xylene, a high demand compound in the chemical market, could also be produced  
283 through catalytic transalkylation of toluene with TMB [30].

284 Among O-containing compounds, two interesting compounds for the fine chemical  
285 industry were observed: furfural and 5-HMF (5-hydroxymethyl furfural). The former is  
286 mainly used as a selective solvent for the refining of lubricating oils and diesel fuels and as  
287 an intermediate chemical in the manufacturing of many solvents, plastics and agrochemicals.  
288 The latter can be converted to a variety of value-added furan compounds and can be used for  
289 the synthesis of polymers as it contains similar structure as aromatics. Synthesis of 5-HMF  
290 from biomass molecules, involves hydrolysis of the polymeric carbohydrates, isomerization  
291 of glucose into fructose and finally dehydration to 5-HMF [31].

292 **Figure 4** shows the selectivity towards furans, furfural and 5-HMF. From the figure it  
293 is evident that 5-HMF was promoted by all catalysts since a complete absence of this

294 compound was observed in the thermal reaction. Approximately 50% of furans corresponded  
295 to furfural and 5-HMF. Similarly to hydrocarbons, Ni(5)Z was the most active catalyst in  
296 favoring the formation of 5-HMF. In the chemical pathway for cellulose transformation to 5-  
297 HMF, Brønsted acidity is believed to promote the depolymerization of oligosaccharides to  
298 monomeric anhydro-sugars [32]. The isomerization to fructose seems to occur in the presence  
299 of LAS and the dehydration is thought to be promoted by BAS [33].

### 300 **3.4. Catalyst deactivation**

301 Coke nature of spent catalysts was studied by FTIR spectroscopy (**Figure 5a**). An  
302 intense band at  $3434\text{ cm}^{-1}$  could be observed in all samples. That band is attributed to bridging  
303 hydroxyl groups, while the smaller band at  $3234\text{ cm}^{-1}$  is attributed to H-bonding between  
304 acidic hydroxyl groups and adsorbed molecules. The bands between  $2800\text{--}3000\text{ cm}^{-1}$  are  
305 attributed to the CH stretching modes (symmetric and asymmetric) of  $\text{CH}_3$  groups. The bands  
306 from  $1300\text{--}1700\text{ cm}^{-1}$  can be assigned to the CH bending of paraffinic groups and the CC  
307 stretching modes of unsaturated groups. The bands around  $1450\text{--}1700\text{ cm}^{-1}$  are mainly  
308 attributed to aromatics structure vibration [34]. **Figure 5b** shows FTIR spectroscopy of fresh  
309 HZ where a total absence of carbon signals was observed.

310 Catalyst stability was evaluated with six consecutive reaction cycles. Since products  
311 yields (biooil, biochar and gases) did not suffer significant variations, six main compounds,  
312 including furans and aromatics, were chosen to test the zeolite deactivation. The most active  
313 catalyst -Ni(5)Z- was selected and its re-uses are presented in **Figure 6**. Results showed  
314 partially deactivation just in the second cycle. This behavior can be explained by coke

315 deposition. From **Table 1**, it could be observed how  $S_{\text{BET}}$  decreased in all spent catalysts. In  
316 the case of Ni(5)Z, an area loss of about  $100 \text{ m}^2 \text{ g}^{-1}$  was obtained after the first use.

317 From **Figure 6** it is possible to confirm an increment on furfural selectivity as reuses  
318 cycles advanced. However, the other compounds analyzed were reduced (Selectivities  $< 1$   
319 wt%). This behavior could be explained by the surface area reduction previously commented.  
320 When zeolites pores were physically blocked by coke deposition, pyrolysis products could  
321 not get in contact with the catalyst active sites. Thus, reaction products resulted to be quiet  
322 similar to non-catalytic reactions. Besides, Renzini et al. [19] found that coke deposition over  
323 ZMS-11 zeolites caused a decrease of both BAS and LAS.

324 However, it is noteworthy that upon deactivation Ni(5)Z could be easily regenerated  
325 by calcination. After that, catalytic activity was completely recovered. **Figure S1** presents  
326 XRD pattern of the regenerated catalyst, confirming ZSM-11 structure and crystallinity.  
327 Coke deposition resulted in a temporarily catalyst poisoning and acid sites blockage that  
328 could be thermally solved.

### 329 **3.5. Activated biochars characterization**

330 **Table 3** presents physicochemical characteristics of the synthesized AB samples.  
331 Biochar is presented for comparison reasons. As can be observed,  $S_{\text{BET}}$  doubled when the  
332 KOH:biochar ratio increased from 1:1 to 3:1. In general, BET surface area increases when  
333 KOH content or temperature increase [12,35]

334 Proximate analysis revealed that fixed carbon in the activated biochars was higher than  
335 in the starting biomass, which resulted from an effective carbonization process [36]. As the  
336 temperature increases, it is expected that the carbon content increases and that of the volatiles

337 decreases, since devolatilization processes predominantly occur [37]. From the analysis of  
 338 activated materials, it could be observed that the fixed carbon content decreased as the surface  
 339 area increased, thus registering AB 3:1 sample the lowest fixed carbon value. Moisture  
 340 content in this sample was almost 4% higher, suggesting that it is slightly more hygroscopic  
 341 than AB 1:1.

**Table 3.** Physicochemical characteristics of activated biochars.

	Proximate analysis (%w/w) <sup>a</sup>				S <sub>BET</sub> (m <sup>2</sup> g <sup>-1</sup> )
	Moisture	Volatile matter	Fix carbon	Ash	
Biochar	6.83	27.95	58.69	6.53	215
AB 1:1	20.11	10.97	64.45	4.47	832
AB 3:1	23.89	12.6	58.51	5	1645

342 <sup>a</sup> Determined by TGA.

343 XRD diffractograms and Raman spectra display the crystallographic structures of the  
 344 activated materials (**Figure 7**). All specimens presented a broad band located at  $2\theta = 20-30^\circ$   
 345 which is characteristic of amorphous materials, suggesting the existence of amorphous  
 346 carbon caused by incomplete carbonization [38]. The peak at  $2\theta = 23.5^\circ$  corresponds to the  
 347 (002) graphite planes. From **Figure 7a** it can be observed that this broad peak is stronger in  
 348 biochar and weaker in the AB samples, proving an increase in the degree of graphitization.  
 349 **Figure 7b** presents Raman spectra of the as-prepared porous carbon materials. The D-bands  
 350 ( $\sim 1356\text{ cm}^{-1}$ ) and G-bands ( $\sim 1604\text{ cm}^{-1}$ ) correspond to the disordered carbon and graphite  
 351 carbon, respectively [39]. D and G bands ratio ( $I_D/I_G$ ) changed from 0.959 in pyrolysis

352 biochar to 0.999 in AB 3:1 sample, indicating a higher graphitization degree at a higher  
353 temperature.

354 The FTIR spectra of the AB samples are shown in **Figure 8**. The presence of surface  
355 functional groups is considered an important factor that determines the adsorption behavior  
356 of activated carbons. The vibrations of some functional groups could be observed. The band  
357 at 400-750  $\text{cm}^{-1}$  was assigned to the stretching vibration of C-C and the one at 750-900  $\text{cm}^{-1}$   
358 was responsible for the bending of C-H. The signals at 1050  $\text{cm}^{-1}$  and 1250  $\text{cm}^{-1}$  were  
359 attributed to the vibrations of C-O and C-O-C and the peak at 1480  $\text{cm}^{-1}$  would indicate the  
360 stretching vibration C=C [35]. The signal at 1700  $\text{cm}^{-1}$  was assigned to the C=O stretch and  
361 the one at 1750  $\text{cm}^{-1}$  resulted from the presence of -COOH groups. While the band at 2800-  
362 2900  $\text{cm}^{-1}$  was responsible for the stretching of aliphatic CH, the broad band at 3400  $\text{cm}^{-1}$   
363 was assigned to the vibration of -OH, corresponding to adsorbed water molecules [35,40].

364 SEM micrographs of the as-prepared materials are presented in **Figure 9**. AB 1:1  
365 sample presented a rib-like structure (**Fig. 9a**) on which the presence of numerous dispersed  
366 pores could be observed. As the KOH content increased, the precursor (biochar) continued  
367 decomposing, and the formation of many new macropores could be observed in AB 3:1  
368 sample (**Fig. 9b**). Thus indicating that the ribs observed in AB 1:1 were transformed into  
369 channels in AB 3:1. Consequently, the opening of the macropores possibly contributed to the  
370 formation of new micro and mesopores on the internal surfaces.

#### 371 **4. Conclusions**

372 With aims for a circular bioeconomy, the valorization and recycling of PS in two  
373 subsequent product systems was studied. The first system consisted of catalytic fast pyrolysis

374 of the residual biomass where a group of Ni-ZSM-11 matrices was tested. When varying Ni  
375 content, a surface area reduction was obtained, but acid sites were improved. From the  
376 evaluated materials, Ni(5)Z showed the best results in terms of hydrocarbons and platform  
377 molecules selectivities. This catalyst was further measured in terms of stability over several  
378 reaction cycles. The temporary poisoning was easily solved by calcination, after which the  
379 material recovered its pristine crystallinity and catalytic behavior. Thus, it is possible to  
380 affirm that nickel ZSM-11 zeolites with a 5 wt% of loading are ideal catalysts for the  
381 pyrolytic conversion of peanut shell to interesting platform molecules.

382         The second system consisted of synthesizing AB employing the residual biochar from  
383 the previous pyrolysis as the precursor. The materials were produced by a simple thermo-  
384 chemical procedure, employing KOH as activation agent. Surface area ( $S_{\text{BET}}$ ) could be  
385 significantly increased upon activation, from 215 m<sup>2</sup>/g in biochar to 1645 m<sup>2</sup>/g when  
386 KOH:biochar ratio was 3:1. Considering the type and quantity of surface functional groups  
387 found on these materials, they could be used for a variety of sorption processes.

388         These results proved to be an example of an efficient biobased renewable resource  
389 management.

### 390 **Associated content**

391         File name: Fermanelli et al. – Supporting Information. File format: .docx.

392         Data: XRD pattern of regenerated Ni(5)Z. Main compounds detected in bio-oils by  
393 CG-MS analysis.

### 394 **Declarations**

395 **Availability of data and materials**

396 All data generated or analyzed during this study are available from the corresponding  
397 author, upon reasonable request. The necessary data that were generated and analyzed during  
398 the study are included in this published article.

399 **Competing interests**

400 The authors declare they have no competing interest.

401 **Author Contributions**

402 Carla S. Fermanelli: investigation, methodology, data curation, writing – original draft.  
403 Adrián Chiappori: resources. Liliana Pierella: project administration. Clara Saux:  
404 conceptualization, writing – review and editing, supervision. All authors have given approval  
405 to the final version of the manuscript.

406 **Acknowledgements**

407 The authors of this work would like to thank Universidad Tecnológica Nacional (PID  
408 UTN 6562), Ministerio de Ciencia y Tecnología de Córdoba (PIOdo18) and Consejo  
409 Nacional de Investigaciones Científicas y Técnicas (CONICET).

410 **Authors' information.**

411 **Corresponding author**

412 Carla S. Fermanelli – Unidad de Fitopatología y Modelización Agrícola (UFYMA) –  
413 INTA – CONICET, Camino 60 Cuadras km 5 1/2, Córdoba, Argentina;  
414 <https://orcid.org/0000-0003-3136-5187>; Email: [cfermanelli@frc.utn.edu.ar](mailto:cfermanelli@frc.utn.edu.ar).

415 **Authors**

416 Adrián Chiappori – Centro de Investigación y Tecnología Química (CITeQ) –  
417 CONICET – UTN, Maestro López esq. Cruz Roja Argentina (5016), Córdoba, Argentina.  
418 Email: [achiappori@frc.utn.edu.ar](mailto:achiappori@frc.utn.edu.ar)

419 Liliana B. Pierella – Centro de Investigación y Transferencia en Acústica (CINTRA) –  
420 CONICET – UTN, Maestro López esq. Cruz Roja Argentina (5016), Córdoba, Argentina.  
421 Email: [lpierella@frc.utn.edu.ar](mailto:lpierella@frc.utn.edu.ar)

422 Clara Saux – Centro de Investigación y Tecnología Química (CITeQ) – CONICET –  
423 UTN, Maestro López esq. Cruz Roja Argentina (5016), Córdoba, Argentina.  
424 <https://orcid.org/0000-0002-4324-8490>; Email: [csaux@frc.utn.edu.ar](mailto:csaux@frc.utn.edu.ar).

425

426 **References**

427 [1] R. Kapoor, P. Ghosh, M. Kumar, S. Sengupta, A. Gupta, S.S. Kumar, V. Vijay, V. Kumar,  
428 V. Kumar Vijay, D. Pant, *Bioresour. Technol.* 304 (2020) 123036.

429 [2] E. Hadley Kershaw, S. Hartley, C. McLeod, P. Polson, *Trends Biotechnol.* xx (2020) 1–4.

430 [3] Food and Agriculture Organization, (2021).

431 [4] C.S. Fermanelli, E.D. Galarza, L.B. Pierella, M.S. Renzini, C. Saux, *Top. Catal.* 62 (2019).

432 [5] C.S. Fermanelli, A. Córdoba, L.B. Pierella, C. Saux, *Waste Manag.* 102 (2020).

433 [6] L. Dai, Y. Wang, Y. Liu, R. Ruan, D. Duan, Y. Zhao, Z. Yu, L. Jiang, *Bioresour. Technol.*  
434 272 (2019) 407–414.

- 435 [7] T. Kan, V. Strezov, T. Evans, J. He, R. Kumar, Q. Lu, *Renew. Sustain. Energy Rev.* 134  
436 (2020) 110305.
- 437 [8] J. Olofsson, P. Börjesson, *J. Clean. Prod.* 196 (2018) 997–1006.
- 438 [9] E.D. Galarza, C.S. Fermanelli, L.B. Pierella, C. Saux, M.S. Renzini, *J. Anal. Appl. Pyrolysis*  
439 156 (2021) 105116.
- 440 [10] C.A. Emeis, *J. Catal.* 141 (1993) 347–354.
- 441 [11] A. Aho, N. Kumar, K. Eränen, T. Salmi, M. Hupa, D.Y. Murzin, *Fuel* 87 (2008) 2493–2501.
- 442 [12] Y. Fu, Y. Shen, Z. Zhang, X. Ge, M. Chen, *Sci. Total Environ.* 646 (2019) 1567–1577.
- 443 [13] J.F. Saldarriaga, R. Aguado, A. Pablos, M. Amutio, M. Olazar, J. Bilbao, *Fuel* 140 (2015)  
444 744–751.
- 445 [14] E.F. Iliopoulou, S.D. Stefanidis, K.G. Kalogiannis, A. Delimitis, A.A. Lappas, K.S.  
446 Triantafyllidis, *Appl. Catal. B Environ.* 127 (2012) 281–290.
- 447 [15] N. Brodu, M.H. Manero, C. Andriantsiferana, J.S. Pic, H. Valdés, *Chem. Eng. J.* 231 (2013)  
448 281–286.
- 449 [16] L. Li, C. Stroobants, K. Lin, P.A. Jacobs, B.F. Sels, P.P. Pescarmona, *Green Chem.* 13  
450 (2011) 1175–1181.
- 451 [17] A. Kostyniuk, D. Key, M. Mdleleni, *J. Energy Inst.* 5 (2019) 1–13.
- 452 [18] A. Kostyniuk, D. Bajec, B. Likozar, *Renew. Energy* (2020).
- 453 [19] M.S. Renzini, L.C. Lericci, U. Sedran, L.B. Pierella, *J. Anal. Appl. Pyrolysis* 92 (2011) 450–  
454 455.
- 455 [20] Z.P. Hu, C.C. Weng, C. Chen, Z.Y. Yuan, *Appl. Catal. A Gen.* 562 (2018) 49–57.

- 456 [21] M.A. Zanjanchi, A. Razavi, *Spectrochim. Acta - Part A Mol. Biomol. Spectrosc.* 57 (2001)  
457 119–127.
- 458 [22] X. Li, D. Han, H. Wang, G. Liu, B. Wang, Z. Li, J. Wu, *Fuel* 144 (2015) 9–14.
- 459 [23] I. Graça, L. V. González, M.C. Bacariza, A. Fernandes, C. Henriques, J.M. Lopes, M.F.  
460 Ribeiro, *Appl. Catal. B Environ.* 147 (2014) 101–110.
- 461 [24] A.R. Stanton, K. Iisa, M.M. Yung, K.A. Magrini, *J. Anal. Appl. Pyrolysis* 135 (2018) 199–  
462 208.
- 463 [25] P.S. Rezaei, H. Shafaghat, W.M.A.W. Daud, *Appl. Catal. A Gen.* 469 (2014) 490–511.
- 464 [26] X. Ren, H. Cai, Q. Zhang, D. Zhang, X. Lin, *Energy* 214 (2021) 118799.
- 465 [27] A. Veses, B. Puértolas, M.S. Callén, T. García, *Microporous Mesoporous Mater.* 209 (2015)  
466 189–196.
- 467 [28] J.A. Botas, D.P. Serrano, A. García, J. De Vicente, R. Ramos, *Catal. Today* 195 (2012) 59–  
468 70.
- 469 [29] Y. Cai, Y. Fan, X. Li, L. Chen, J. Wang, *Energy* 102 (2016) 95–105.
- 470 [30] F.M. Almulla, S.A. Ali, M.R. Aldossary, E.I. Alnaimi, A. bin Jumah, A.A. Garforth, *Appl.*  
471 *Catal. A Gen.* 608 (2020) 117886.
- 472 [31] I.K.M. Yu, D.C.W. Tsang, A.C.K. Yip, S.S. Chen, Y.S. Ok, C.S. Poon, *Bioresour. Technol.*  
473 219 (2016) 338–347.
- 474 [32] H. Zhang, X. Liu, M. Lu, X. Hu, L. Lu, X. Tian, J. Ji, *Bioresour. Technol.* 169 (2014) 800–  
475 803.
- 476 [33] A.A. Marianou, C.M. Michailof, A. Pineda, E.F. Iliopoulou, K.S. Triantafyllidis, A.A.  
477 Lappas, *Appl. Catal. A Gen.* 555 (2018) 75–87.

- 478 [34] N. Chaouati, A. Soualah, M. Chater, M. Tarighi, L. Pinard, *J. Catal.* 344 (2016) 354–364.
- 479 [35] Y. Shen, Y. Zhou, Y. Fu, N. Zhang, *Renew. Energy* 146 (2020) 1700–1709.
- 480 [36] J.K. Ratan, M. Kaur, B. Adiraju, *Mater. Today Proc.* 5 (2018) 3334–3345.
- 481 [37] N.A. Rashidi, S. Yusup, M.M. Ahmad, N.M. Mohamed, B.H. Hameed, *APCBEE Procedia* 3  
482 (2012) 84–92.
- 483 [38] H. Lin, Y. Liu, Z. Chang, S. Yan, S. Liu, S. Han, *Microporous Mesoporous Mater.* 292  
484 (2020) 109707.
- 485 [39] C. Guo, R. Hu, W. Liao, Z. Li, L. Sun, D. Shi, Y. Li, C. Chen, *Electrochim. Acta* 236 (2017)  
486 228–238.
- 487 [40] J. Lee, X. Yang, S.H. Cho, J.K. Kim, S.S. Lee, D.C.W. Tsang, Y.S. Ok, E.E. Kwon, *Appl.*  
488 *Energy* 185 (2017) 214–222.

#### 489 **Figure legends**

490 **Figure 1.** Schematic illustration of open-loop recycling between three systems. Adapted  
491 from Olofsson and Börjesson [8].

492 **Figure 2. a)** FTIR spectra (L: Lewis; B: Brønsted) **b)** XRD patterns, **c)** TPR profiles and **d)**  
493 UV-vis DR spectra of Ni-zeolites.

494 **Figure 3.** Selectivity towards **a)** oxygenated compounds, **b)** hydrocarbons and **c)** C-atoms  
495 per molecule of hydrocarbon in biooils from PS pyrolysis catalyzed by Ni-zeolites.

496 **Figure 4.** Selectivity towards furans, furfural and 5-HMF in biooils from PS pyrolysis  
497 catalyzed by Ni-zeolites.

498 **Figure 5.** FTIR spectra of **a)** spent catalysts and **b)** fresh HZ catalyst. Dash squares  
499 emphasize lack of carbon signals.

500 **Figure 6.** Compounds selectivity in consecutive cycles of PS pyrolysis over Ni(5)Z.

501 **Figure 7. a)** XRD patterns and **b)** Raman spectra of activated biochars.

502 **Figure 8.** FTIR spectra of activated biochars.

503 **Figure 9.** SEM micrographs of activated biochars. **a)** AB 1:1, **b)** AB 3:1.

# Figures

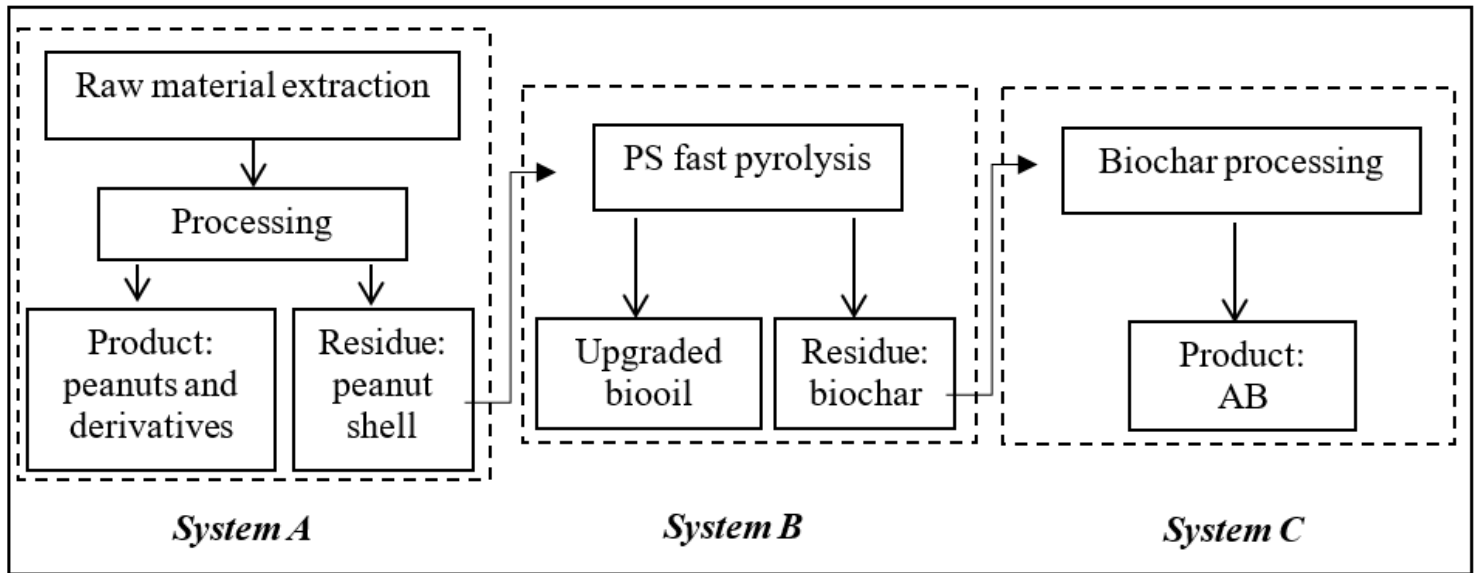
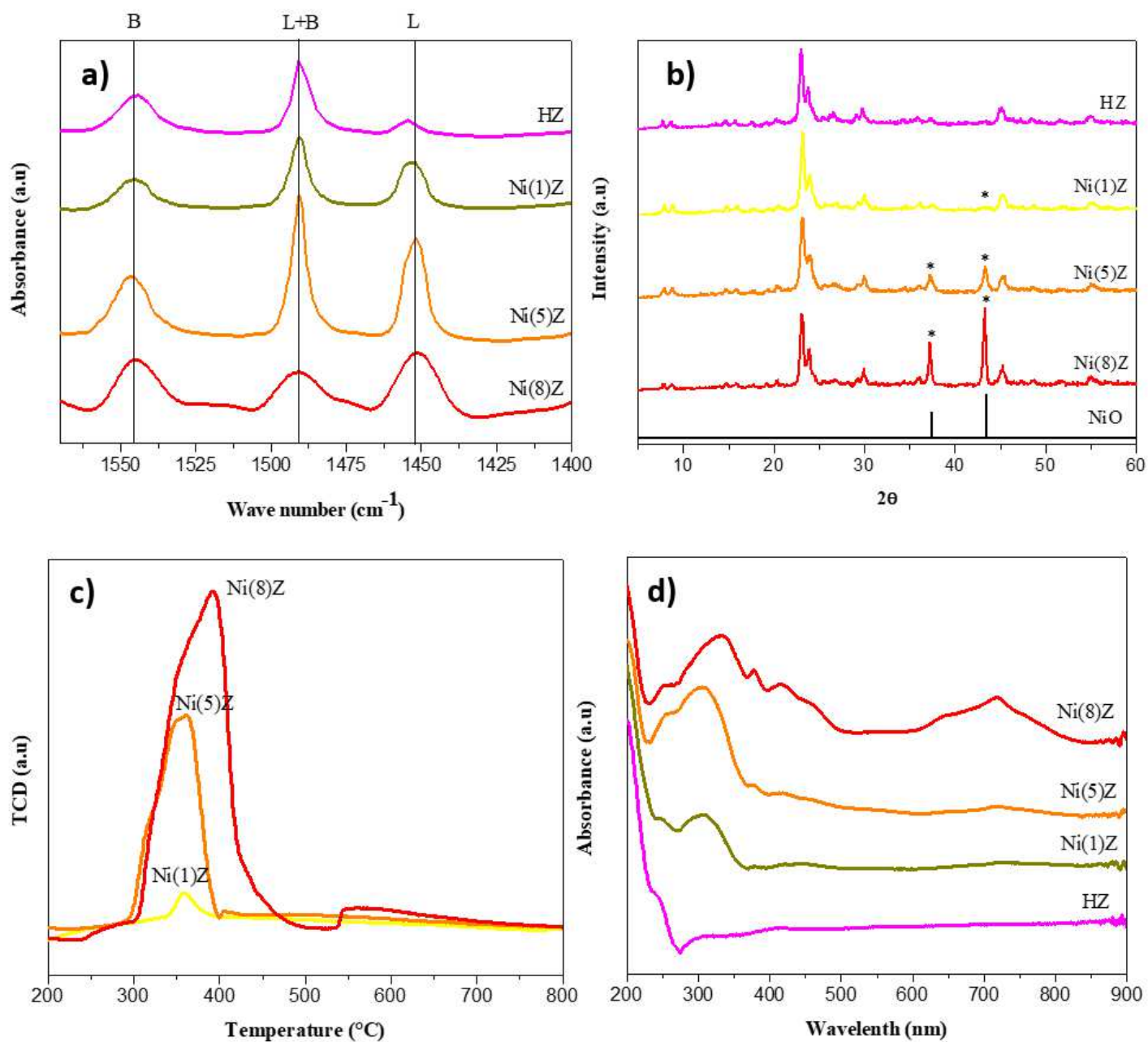


Figure 1

Schematic illustration of open-loop recycling between three systems. Adapted from Olofsson and Börjesson [8].



**Figure 2**

a) FTIR spectra (L: Lewis; B: Brønsted) b) XRD patterns, c) TPR profiles and d) UV-vis DR spectra of Ni-zeolites.

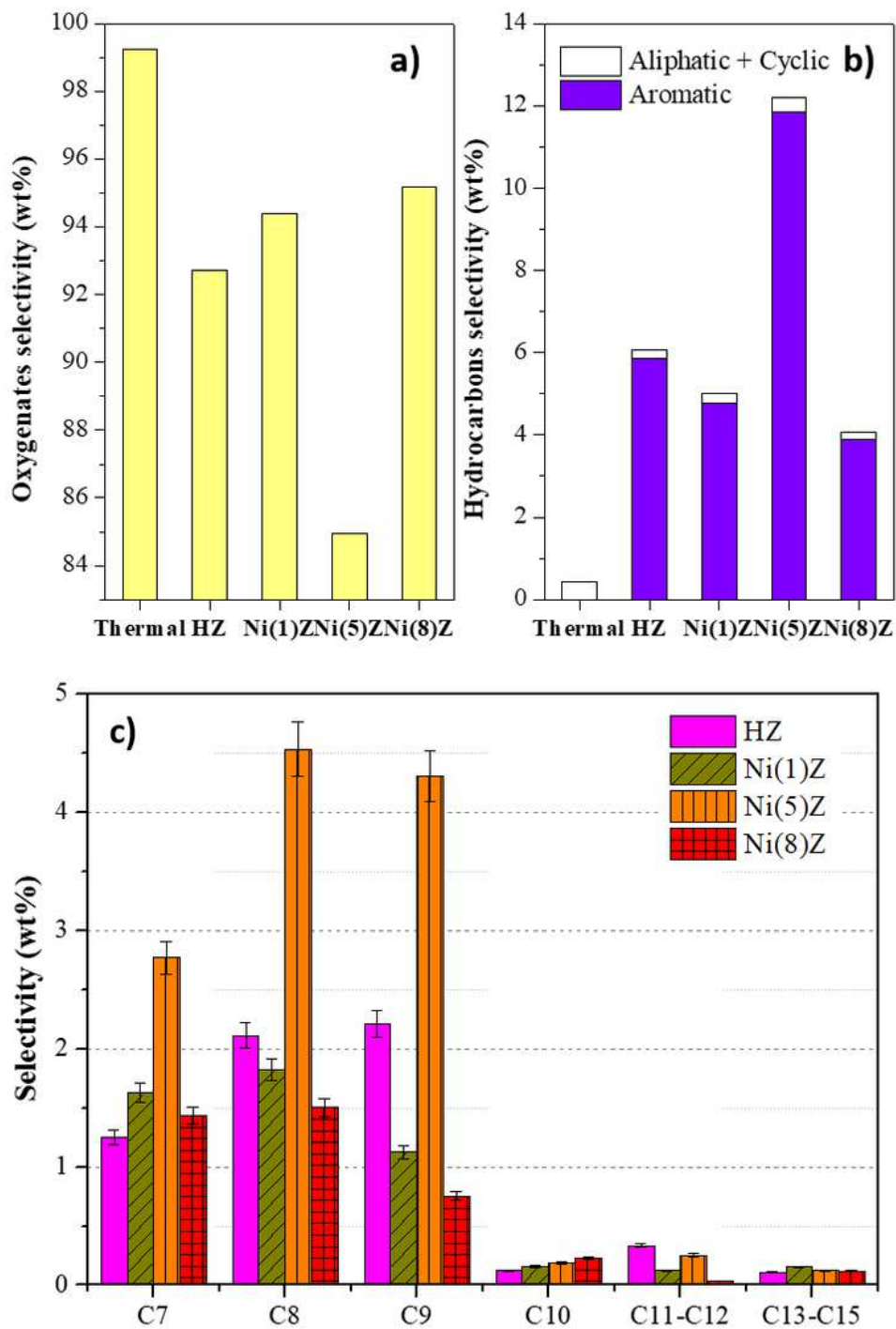


**Figure 3**

Selectivity towards a) oxygenated compounds, b) hydrocarbons and c) C-atoms per molecule of hydrocarbon in biooils from PS pyrolysis catalyzed by Ni-zeolites.

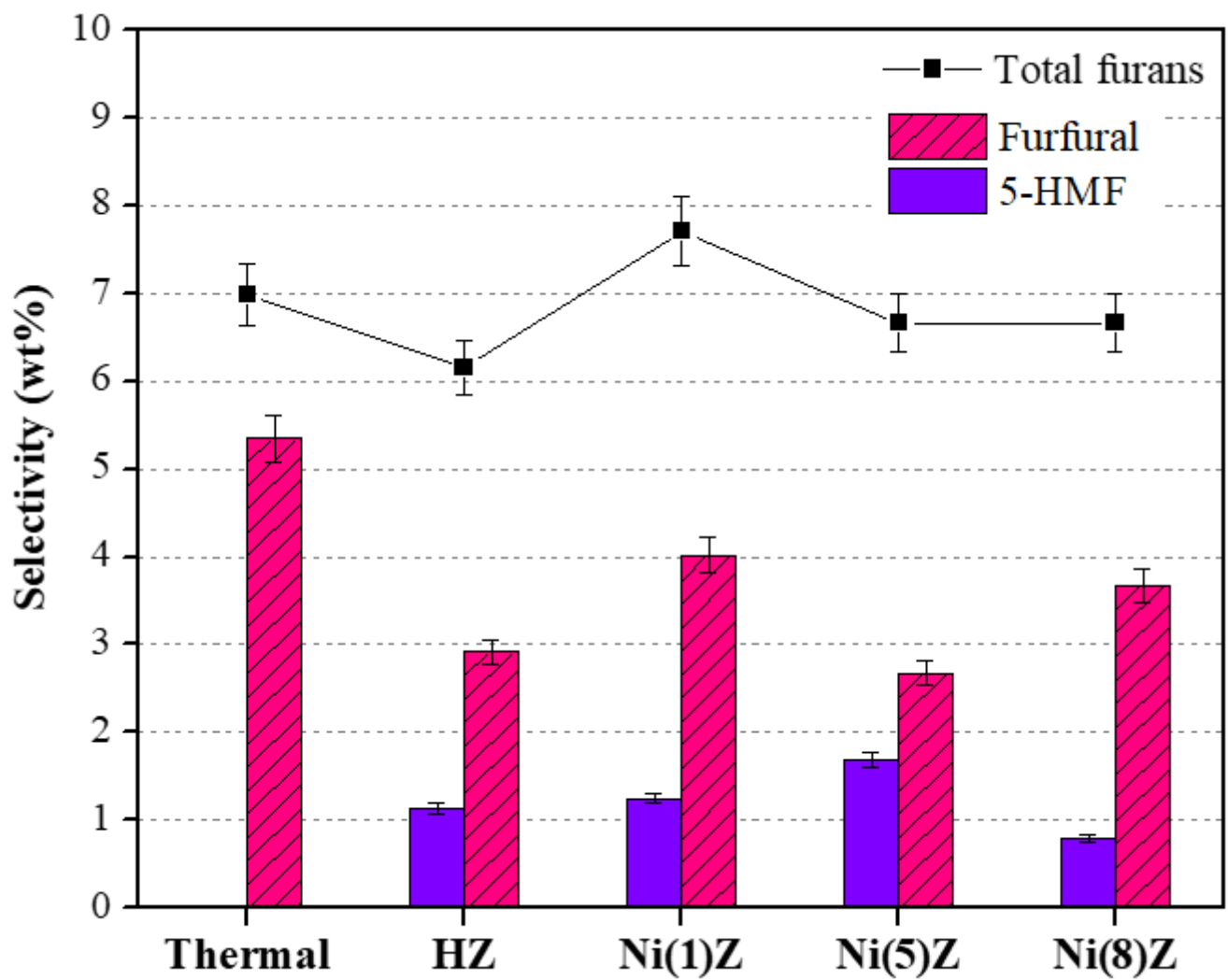
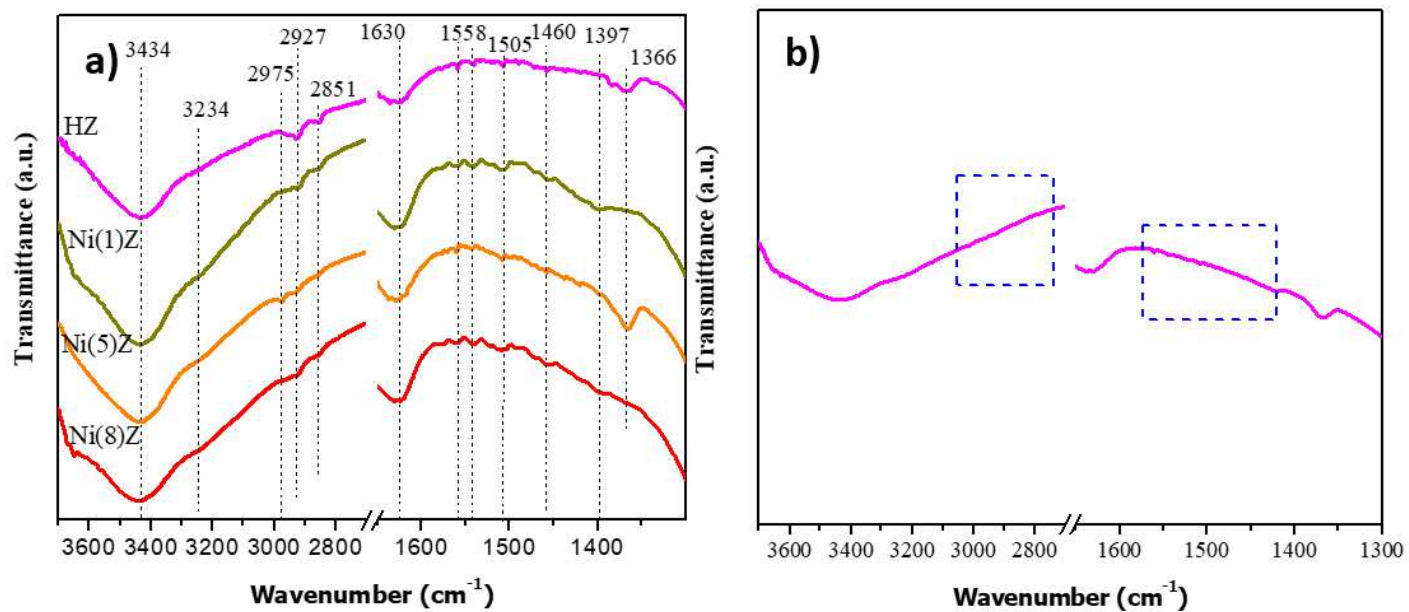


Figure 4

Selectivity towards furans, furfural and 5-HMF in biooils from PS pyrolysis catalyzed by Ni-zeolites.



**Figure 5**

FTIR spectra of a) spent catalysts and b) fresh HZ catalyst. Dash squares emphasize lack of carbon signals.

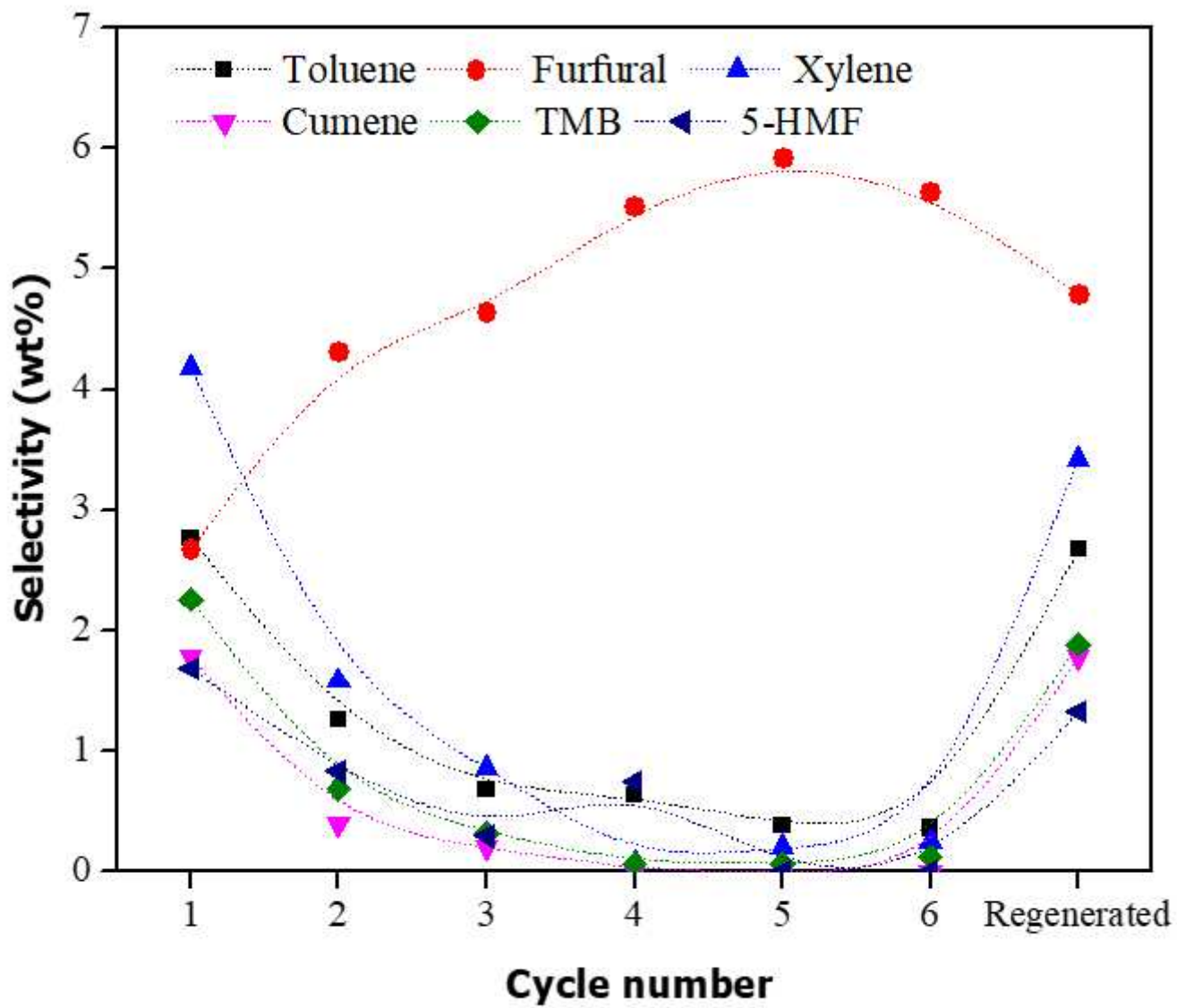


Figure 6

Compounds selectivity in consecutive cycles of PS pyrolysis over Ni(5)Z.

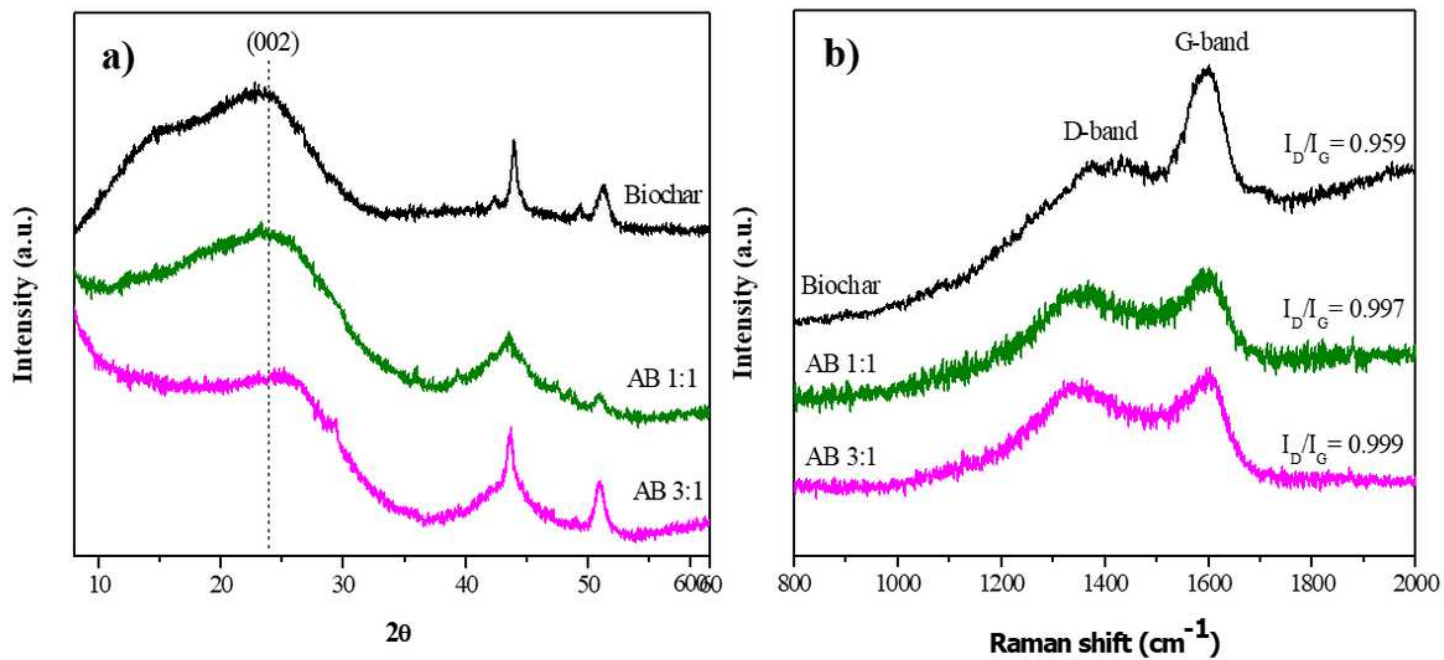


Figure 7

a) XRD patterns and b) Raman spectra of activated biochars.

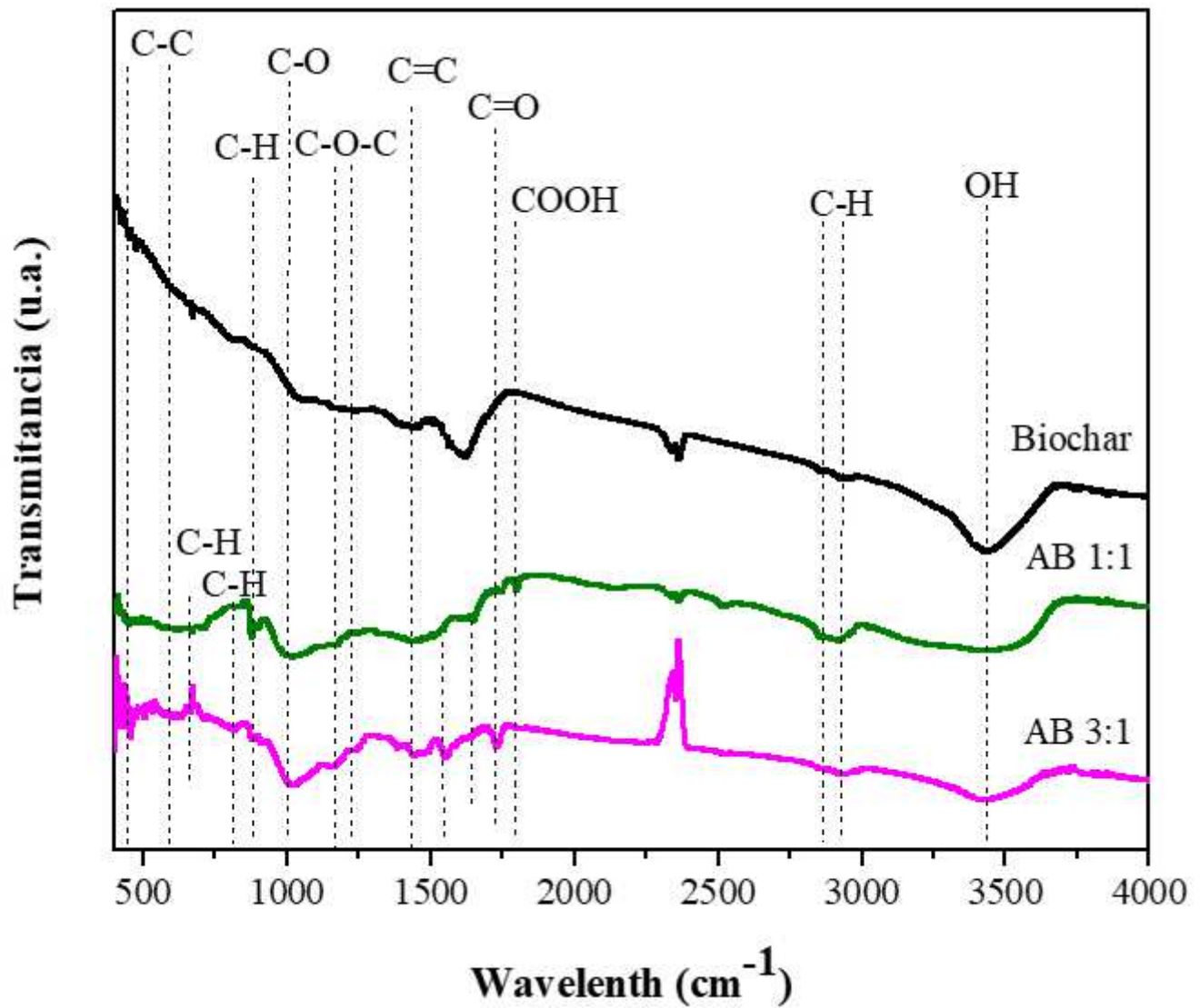
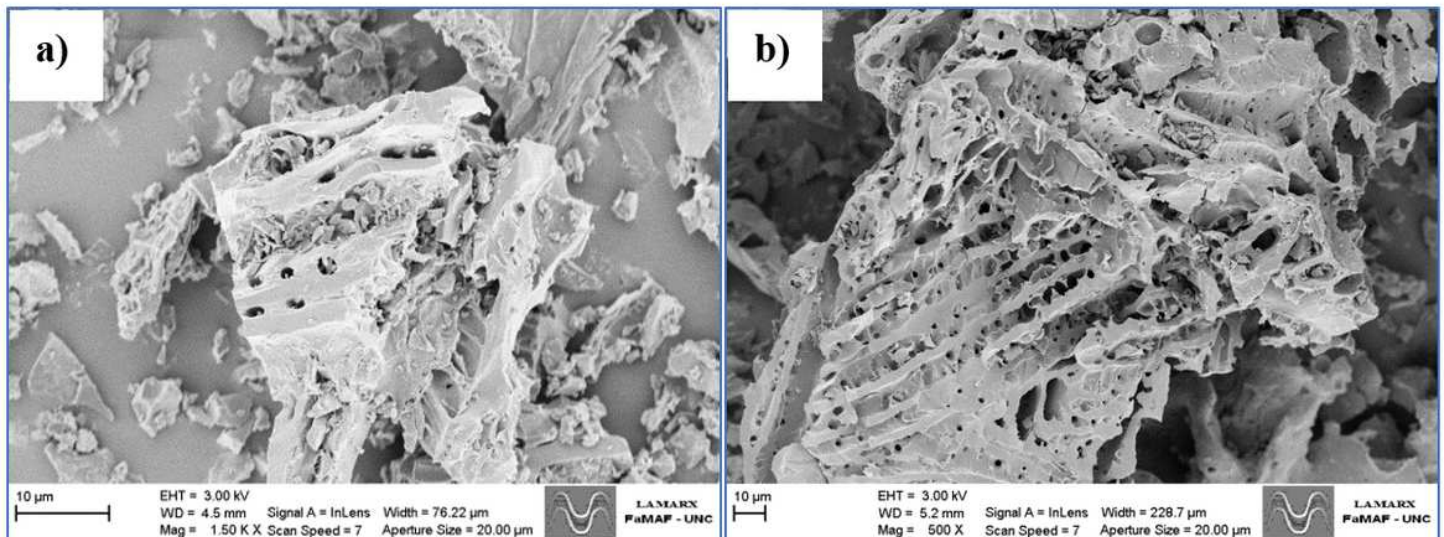


Figure 8

FTIR spectra of activated biochars.



## Figure 9

SEM micrographs of activated biochars. a) AB 1:1, b) AB 3:1.

## Supplementary Files

This is a list of supplementary files associated with this preprint. Click to download.

- [Fermanellietal.SupportingInformation.docx](#)